

# Generative Inverse Design of Cold Metals for Low-Power Electronics

Kedeng Wu<sup>a</sup>, Yucheng Zhu<sup>a</sup>, Yan Chen<sup>b</sup>, Bizhu Zhang<sup>a</sup>, Shuyu Liu<sup>a</sup>, Xiaobin Deng<sup>c</sup>, Yabei Wu<sup>d,\*</sup>,  
Liangliang Zhu<sup>a,\*</sup>, Hang Xiao<sup>c,\*</sup>

<sup>a</sup> School of Chemical Engineering, Northwest University, Xi'an 710127, China

<sup>b</sup> Laboratory for Multiscale Mechanics and Medical Science, SV LAB, School of Aerospace, Xi'an  
Jiaotong University, Xi'an 710049, China

<sup>c</sup> Wu Jieh Yee School of Interdisciplinary Studies, Lingnan University, Tuen Mun, Hong Kong SAR,  
China

<sup>d</sup> Department of Materials Science and Engineering and Guangdong Provincial Key Lab for  
Computational Science and Materials Design, Southern University of Science and Technology, Shenzhen,  
Guangdong 518055, China

\*E-mail: [wuyb3@sustech.edu.cn](mailto:wuyb3@sustech.edu.cn), [zhu.liangliang@nwu.edu.cn](mailto:zhu.liangliang@nwu.edu.cn), [hangxiao@ln.edu.hk](mailto:hangxiao@ln.edu.hk).

# Abstract

Cold metals are a class of metals with an intrinsic energy gap located close to the Fermi level, which enables cold-carrier injection for steep-slope transistors and is therefore promising for low-power electronic applications. High-throughput screening has revealed 252 three-dimensional (3D) cold metals in the Materials Project database, but database searches are inherently limited to known compounds. Here we present an inverse-design workflow that generates 3D cold metals using MatterGPT, a conditional autoregressive Transformer trained on SLICES, an invertible and symmetry-invariant crystal string representation. We curate a training set of 26,309 metallic structures labeled with energy above hull and a unified band-edge distance descriptor that merges p-type and n-type cold-metal characteristics to address severe label imbalance. Property-conditioned generation targeting thermodynamic stability and 50-500 meV band-edge distances produces 148,506 unique candidates; 92.1% are successfully reconstructed to 3D structures and down-selected by symmetry, uniqueness and novelty filters, followed by high-throughput DFT validation. We identify 257 cold metals verified as novel with respect to the Materials Project database, with gaps around the Fermi level spanning 50-500 meV. First-principles phonon, electronic-structure, and work-function calculations for representative candidates confirm dynamical stability and contact-relevant work functions. Our results demonstrate that SLICES-enabled generative transformers can expand the chemical space of cold metals beyond high-throughput screening, providing a route to low-power electronic materials discovery.

**Keywords:** Cold Metals; SLICES; Inverse Design; MatterGPT; Low-Power Electronics.

# Introduction

Power dissipation has become a critical bottleneck in the continued scaling and performance improvement of complementary metal–oxide–semiconductor (CMOS) technology. In conventional metal–oxide–semiconductor field-effect transistors (MOSFETs), the thermionic emission mechanism imposes a fundamental lower bound on the subthreshold swing (SS) of  $\sim 60$  mV/decade at room temperature (300 K), widely referred to as the Boltzmann tyranny [1–4]. This limit constrains the minimum operating voltage required to switch transistors on and off, making further reductions in dynamic power consumption exceedingly difficult. To circumvent this constraint, a variety of steep-slope device concepts have been proposed, including tunnel FETs, negative-capacitance FETs, and impact-ionization devices [1,5–10]. Among these approaches, the cold-source FET (CSFET) has attracted growing interest owing to its conceptual elegance: rather than modifying the channel transport mechanism, it employs a source contact material whose electronic structure inherently filters out high-energy carriers before they are injected into the channel [11,12].

The source material central to this strategy is termed a “cold metal.” First proposed by Liu in 2020 [11], a cold metal is defined as a metallic material that possesses an intrinsic energy gap immediately above and/or below the Fermi level ( $E_F$ ). Unlike a conventional metal, whose continuous density of states (DOS) around  $E_F$  permits carrier occupation at all energies set by the Fermi–Dirac distribution, a cold metal features a DOS gap that suppresses the high-energy tail of the carrier distribution [11,13–15]. This energy-filtering window effectively blocks thermally excited (“hot”) electrons from participating in injection, so that only carriers within a narrow, low-energy window contribute to current flow. When a cold metal is used as the source contact of a transistor, the injected carrier distribution is significantly colder than the Boltzmann distribution, enabling the device to achieve SS values well below the 60 mV/decade thermionic limit at room temperature [11].

Depending on the position of the band-edge gap relative to  $E_F$ , cold metals can be classified into three principal types: p-type, in which the gap lies above  $E_F$  and filters high-energy electrons; n-type, in which the gap lies below  $E_F$  and filters high-energy holes; and np-type, which exhibits gaps on both sides of  $E_F$  and can filter both carrier types [11,16]. The original proposal by Liu demonstrated the concept using two-dimensional (2D) transition-metal dichalcogenide (TMD) metals— $\text{NbX}_2$  and  $\text{TaX}_2$  ( $X = \text{S}, \text{Se}, \text{Te}$ )—whose electronic structures contain a gap above  $E_F$ , and quantum transport simulations showed that the resulting CSFETs could achieve promising

switching efficiency with reduced power dissipation [11]. Subsequently, Zhang et al. extended the cold-metal paradigm to three-dimensional (3D) bulk materials, exploring TMD sulfides and oxides as cold-source contacts for monolayer MoS<sub>2</sub> transistors. Their simulations demonstrated that 3D cold-metal-contacted MoS<sub>2</sub> FETs can achieve an average SS of ~20 mV/decade over five decades of current and on-state currents exceeding 570  $\mu\text{A}/\mu\text{m}$  [12].

Despite these encouraging results, early studies examined only a handful of cold-metal candidates. To systematically map the landscape of 3D cold metals, Zhang and Liu conducted a high-throughput computational screening of the Materials Project database, evaluating 133,693 entries and identifying 252 3D cold metals whose band-edge gaps fall within the technologically relevant window of 50-500 meV from the Fermi level [16]. Among these, 115 are p-type, 56 are n-type, and 81 are np-type. First-principles calculations on a subset of 30 representative materials revealed several distinctive physical characteristics. First, owing to the suppressed DOS near  $E_F$ , the electrical conductance of cold metals is systematically lower than that of conventional metals, consistent with their energy-filtering function. Second, depending on their specific band-edge gap characteristics, these cold metals exhibit highly tunable work functions that span an extensive range from 2.69 eV to 6.44 eV. This wide tunability provides significant leverage for optimizing energy band alignments at diverse metal–semiconductor interfaces [16]. Third, the thermoelectric properties of cold metals are markedly superior to those of ordinary metals: the Seebeck coefficients of representative materials such as ZrRuSb, RbCu<sub>4</sub>S<sub>3</sub>, CoSi, and Sr<sub>5</sub>Pb<sub>3</sub>F are one to two orders of magnitude larger, and the thermoelectric figure of merit  $zT$  reaches up to 0.6 at 1000 K for Sr<sub>5</sub>Pb<sub>3</sub>F [16]. Moreover, device-level simulations of a monolayer MoS<sub>2</sub> CSFET with a ZrRuSb cold-metal contact demonstrated SS < 60 mV/decade over four decades of current and an on-state current exceeding 1 mA/ $\mu\text{m}$  at a supply voltage of 0.5 V, confirming the practical viability of 3D cold metals for low-power transistor applications [16].

Although this high-throughput screening effort established the first comprehensive dataset of 3D cold metals, it remains fundamentally constrained to materials already catalogued in existing crystallographic databases [17–20]. The accessible chemical and structural space is therefore bounded by prior experimental synthesis and computational enumeration, leaving a vast terra incognita of potential cold metals unexplored. Overcoming this limitation requires a paradigm shift from forward screening—which searches known materials for target properties—to inverse design strategies that directly generate novel crystal structures with prescribed electronic characteristics [21,22].

Recent advances in generative artificial intelligence, particularly Transformer-based large language models, have opened new avenues for property-driven materials discovery. Current sequence-based approaches primarily rely on direct Crystallographic Information File (CIF) [23] processing or text-conditioned training [24], such as the AtomGPT [25] framework, to capture structure-property relationships. These methods show promising capabilities in forward property prediction and generative design. However, they face fundamental limitations in representation and precision. Text-based descriptions and CIF-based sequences suffer from high representational redundancy and are not inherently invariant under translation, rotation, and permutation, typically requiring standardization or augmentation; otherwise, representational redundancy can hinder efficient learning of crystalline symmetries. Additionally, complex natural language prompts hinder the direct, high-precision mapping required to target specific physical properties [26,27].

To overcome the aforementioned limitations in representation methods and generation strategies, this study employs the MatterGPT [28] framework, a Transformer-based generative model that incorporates two distinguishing features. First, it utilizes the Simplified Line-Input Crystal-Encoding System (SLICES) [29] for crystal structure representation. SLICES is a string-based encoding that maintains invertibility and invariance to translational, rotational, and permutational operations, thereby eliminating the representational redundancy inherent in CIF format. Second, the model implements conditional generation by incorporating target property values encoded as continuous property embeddings and concatenated with the SLICES token embeddings. This architecture enables the autoregressive decoder to generate crystal structures conditioned on specified property constraints, facilitating targeted structure prediction for materials with desired characteristics.

We apply this framework to the inverse design of cold metals—to our knowledge, the first generative approach to this emerging materials class—moving beyond database-constrained high-throughput screening. To address the challenge of severe label imbalance from limited cold metal examples, we introduce a unified physical descriptor: the minimum band-edge distance,  $E_{\Delta,min}$ . This descriptor consolidates p-type and n-type cold metal characteristics into a single tractable learning objective. The model was trained on a curated dataset co-labeled with energy above hull and  $E_{\Delta,min}$ .

Property-conditioned generation targeting thermodynamic stability and 50-500 meV band-edge distances produces 148,506 unique SLICES candidates, of which 92.1% are successfully reconstructed into three-dimensional crystal structures. These candidates then undergo a systematic multi-step screening process—novelty assessment against the Materials Project

database [30], symmetry constraint checks, structural uniqueness verification, and high-throughput density functional theory validation of energy above convex hull and electronic properties. This rigorous process yields 257 new cold metals not catalogued in the Materials Project database. These materials exhibit energy gaps around the Fermi level ranging from 50 to 500 meV and energies above the convex hull below 0.25 eV/atom, demonstrating near-hull stability and potential synthesizability. First-principles phonon dispersion calculations confirm dynamical stability of representative candidates, while electronic structure and work function analysis validates their cold metal characteristics and suitability for semiconductor contacts. These results demonstrate that SLICES-enabled generative Transformers can effectively expand the accessible chemical space of cold metals beyond high-throughput screening, providing a computational route to discover low-power electronic materials.

## Methods

### SLICES representation

To enable effective generative modeling of crystalline materials, we employ SLICES, a string-based representation scheme that addresses the fundamental challenges of encoding infinite periodic structures. Similar to how SMILES [31] notation revolutionized molecular informatics by converting molecular graphs into linear strings, SLICES transforms three-dimensional crystal structures into compact, unambiguous text sequences. SLICES possesses two defining characteristics: invertibility, which enables accurate reconstruction of the original structure, and invariance, ensuring that the representation remains unchanged under symmetry operations including translation, rotation, and atom permutation. These characteristics make SLICES particularly well-suited for autoregressive generative models like Transformers [32,33], which excel at learning patterns in sequential data.

The encoding workflow transforms crystalline structures through labeled quotient graphs, finite representations that capture the essential topology and periodicity of infinite lattices. As illustrated in **Fig. 1**, this conversion proceeds in three stages: (1) crystal structure files are parsed into structure objects using Pymatgen [34]. (2) bonding networks are established via the CrystalNN algorithm [35], which identifies atomic connectivity based on coordination environments. (3) the resulting connectivity graph is converted into a SLICES string by encoding elemental composition, node indices for atoms within the unit cell, and critically, edge labels that specify translational periodicity. Each edge is represented as "i j m n p", where indices i and j identify connected atoms,

while the triplet  $m\ n\ p$  defines the lattice translation vector linking unit cells. To prevent ambiguity during parsing, characters 'o', '+', and '-' denote 0, +1, and -1 in edge labels, ensuring numerical digits exclusively indicate node indices. Symmetry information is incorporated by appending a modified Pymatgen "enc"-style space group string to the SLICES representation, where numeric characters are replaced by letters to avoid conflicts with node indices. This encoding scheme elegantly captures both chemical composition and crystallographic periodicity in a format accessible to sequence-based models.

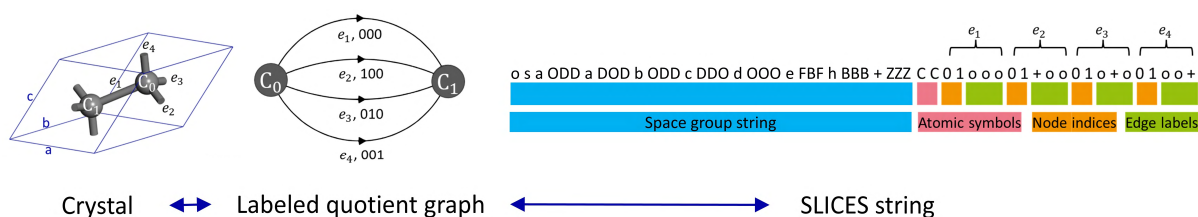


**Fig. 1** | Conversion from a 3D crystal structure to a SLICES string

Reconstruction from SLICES strings to three-dimensional structures is accomplished through the SLI2Cry algorithm, a multi-stage refinement process. Initial structures are generated using Eon's topology-based method, which leverages graph theory and the encoded edge labels to establish correct connectivity and periodicity. These preliminary geometries then undergo optimization based on chemically meaningful geometry predicted with a modified GFN-FF [36] force field, which estimates equilibrium bond lengths and angles. Finally, the M3GNet [37] universal interatomic potential performs structural refinement. Benchmarking on diverse crystal datasets demonstrates that this three-stage approach achieves 94.95% reconstruction success, validating SLICES as a robust foundation for generative materials design.

## MatterGPT architecture

For inverse design of cold metal materials, we employ MatterGPT [28], an autoregressive Transformer architecture operating on SLICES representations. **Fig. 2** illustrates the workflow: during training, the model learns from crystal structures paired with DFT-calculated properties to establish the conditional probability distribution  $P(\text{SLICES}|p_1, \dots, p_n)$ ; during generation, this distribution guides creation of novel SLICES strings conditioned on target properties. Generated strings are reconstructed into crystal structures via SLI2Cry and subjected to computational screening.

MatterGPT adopts a decoder-only architecture with 12 stacked Transformer blocks (**Fig. 2b**). Input SLICES strings undergo preprocessing where a start token '>' is prepended and padding tokens '<' appended to reach uniform length  $N$ . The SLICES vocabulary comprises 132 tokens: 83 atomic symbols, 20 node indices, 27 edge labels, and 2 special tokens. Property specifications  $(p_1, \dots, p_n)$  are concatenated with preprocessed SLICES sequences to form the input. The input representation integrates three embedding components through element-wise summation: token embeddings encoding vocabulary elements, positional embeddings preserving sequential order, and type embeddings distinguishing properties (type = 0) from SLICES tokens (type = 1). Each block contains a masked multi-head self-attention module followed by a feed-forward network, with residual connections and layer normalization applied around each sub-layer. The core self-attention mechanism implements scaled dot-product attention:

$$Attention(Q, K, V) = softmax\left(\frac{QK^T}{\sqrt{d_k}}\right)V \quad (1)$$

where  $Q$ ,  $K$ , and  $V$  represent query, key, and value matrices derived from input embeddings through learned linear transformations, and  $d$  denotes the dimension of the key vectors. The masking mechanism restricts each token to attend only to preceding positions, ensuring autoregressive generation. The architecture employs 12 attention heads operating in parallel, each with 64-dimensional projections. Outputs from all heads are concatenated and linearly transformed, enabling the model to jointly capture information from different representation subspaces. The complete architecture comprises 768-dimensional embeddings and 3072-dimensional feed-forward networks, approximately 80 million trainable parameters.

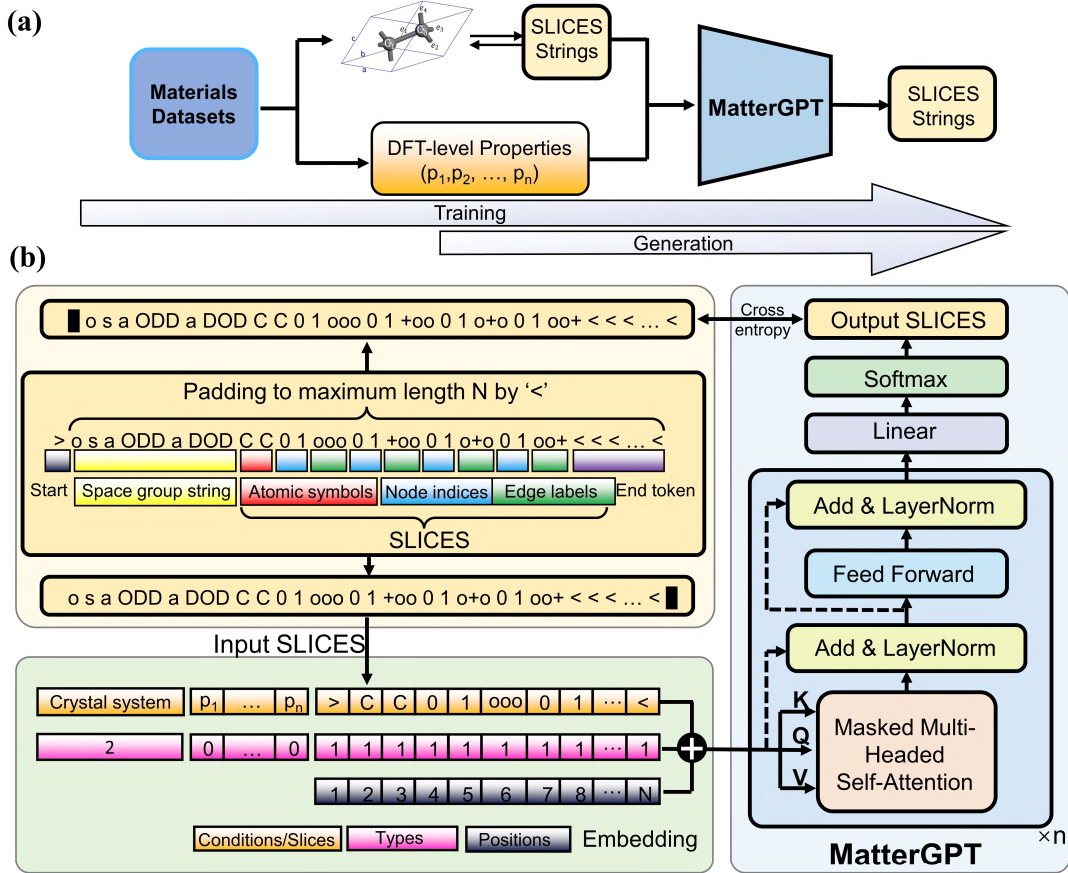


**Fig. 2** | The architecture and workflow of MatterGPT. **(a)** Training and generative sampling pipeline of MatterGPT. **(b)** Detailed model architecture and SLICES string preprocessing workflow. Crystal system, property, and SLICES token embeddings are each assigned type embeddings (0 = properties, 1 = SLICES tokens, 2 = crystal system) to distinguish input modalities, and combined with trainable positional embeddings to capture sequential dependencies.

Training proceeds by maximizing the conditional probability of SLICES sequences given target properties through cross-entropy loss minimization, using the Adam optimizer with a learning rate of 0.0001 and batch size of 60. During generation, Gumbel-Softmax sampling with temperature 1.2 introduces controlled stochasticity to the predicted token distributions. We complement this with nucleus sampling at a cumulative probability threshold of 0.9, restricting token selection to the top 90% probability mass to maintain both generation diversity and property-directed coherence.

## First-principles calculation details

All density functional theory (DFT) [38,39] calculations were performed using the Vienna Ab initio Simulation Package (VASP) [40], employing the projector augmented wave (PAW) method [41] to describe core-valence interactions. The exchange-correlation functional was treated within the generalized gradient approximation (GGA) using the Perdew-Burke-Ernzerhof (PBE) parameterization [42]. To ensure the convergence of total energy, a plane-wave basis set with a kinetic energy cutoff of 520 eV was uniformly applied.

Structural geometry optimization was conducted through a rigorous three-stage relaxation protocol: initially adjusting ionic positions and cell volume, followed by cell shape optimization, and concluding with the refinement of ionic coordinates. This process continued until the residual forces on all atoms converged to less than 0.01 eV/Å. For Brillouin zone integration, we employed Monkhorst-Pack k-point grids generated with a reciprocal space density of 32 to guarantee both computational accuracy and efficiency.

To evaluate the dynamical stability of the identified cold metals, phonon dispersion spectra were computed using the finite displacement method as implemented in the Phonopy package [43]. For these calculations, the kinetic energy cutoff was set to 500 eV, and a stringent energy convergence criterion of  $10^{-8}$  eV was applied to the electronic self-consistency loop to ensure high precision in the resulting force constants.

Furthermore, to assess the electronic energy level alignment critical for device applications, we calculated the work functions ( $\Phi$ ) of representative candidates [44]. Slab models were constructed with a vacuum layer exceeding 15 Å along the surface normal to eliminate spurious interactions between periodic images. The work function was determined via the relation:

$$\Phi = E_{vac} - E_F \quad (2)$$

where  $E_F$  denotes the Fermi level obtained from the electronic structure calculation, and  $E_{vac}$  represents the vacuum energy level obtained from the plateau of the planar-averaged electrostatic potential in the vacuum region.

# Results

## Cold metal screening

Our inverse design workflow begins with the assembly of a comprehensive training dataset from the Materials Project (MP) database [30]. We focused specifically on cold metals, a distinct class of materials characterized by an intrinsic energy gap near the Fermi level. This electronic feature facilitates the effective filtering of high-energy carriers, thereby offering a promising pathway to minimize power dissipation in low-power electronic devices.

Following the classification framework established by Zhang et al. [16], we categorize cold metals into three principal types based on the position of their band-edge gaps relative to the Fermi level, as schematically illustrated by the density of states (DOS) diagrams in **Fig. 3**. p-type cold metals (**Fig. 3a**), analogous to heavily p-doped semiconductors, are characterized by an energy gap positioned above the Fermi level. The key descriptor for this class is  $E_{CD}$ , defined as the energy difference between the conduction band edge of this gap and the Fermi level. n-type cold metals (**Fig. 3b**), which resemble heavily n-doped semiconductors, feature an energy gap located below the Fermi level. Their defining parameter is  $E_{VD}$ , representing the energy difference between the Fermi level and the valence band edge of this gap. np-type cold metals (**Fig. 3c**) exhibit the presence of gaps both above and below the Fermi level and are thus characterized by both an  $E_{CD}$  and an  $E_{VD}$ .

Building on the observation that cold metal properties converge toward conventional metallic behavior as the gap-edge distance increases, we adopt the screening criterion established by Zhang [16]: materials are classified as cold metals when the energy difference between the band-edge gap and the Fermi level falls within the range of 50 meV to 500 meV. This energy window captures the regime where carrier filtering effects are most pronounced while maintaining sufficient metallic conductivity for device applications.

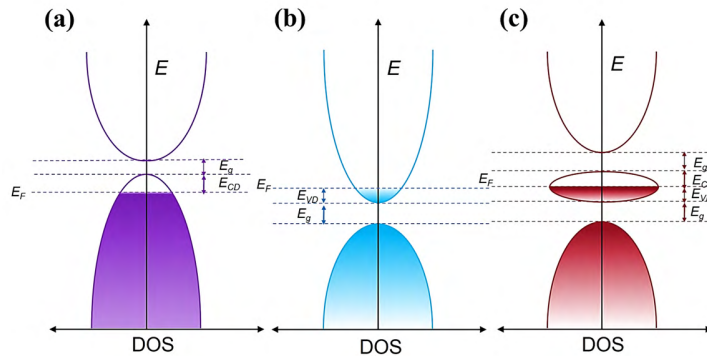


**Fig. 3** | Schematic density of states diagrams illustrating the three principal types of cold metals. **(a)** p-type cold metal, analogous to a heavily p-doped semiconductor, characterized by an energy gap positioned above the  $E_F$ . **(b)** n-type cold metal, analogous to a heavily n-doped semiconductor, exhibiting an energy gap located below  $E_F$ . **(c)** np-type cold metal, featuring energy gaps both above and below  $E_F$ , characterized by both  $E_{CD}$  and  $E_{VD}$ .

To construct the training dataset, we extracted metallic materials from the Materials Project database and applied a rigorous four-step screening protocol:

(1) Only three-dimensional structures were retained, as the labeled quotient graph methodology integral to SLICES encoding is applicable exclusively to 3D periodic crystals.

(2) The dataset was constrained to materials composed of elements with atomic numbers not exceeding 86, accounting for the operational limits of the modified GFN-FF [36] force field in the SLICES reconstruction algorithm. This threshold ensures both stability and accuracy during structural reconstruction.

(3) All non-metallic structures were excluded to focus the analysis exclusively on metallic materials, consistent with the definition of cold metals as a specialized metallic class.

(4) Structures containing more than 20 atoms per unit cell were removed, following established practice in SLICES-based generative modeling frameworks to maintain computational efficiency and training dataset consistency.

These filtering criteria resulted in a final dataset of 26,309 metallic materials. To avoid the data scarcity associated with restricting the study to known cold metals, we included all metallic structures and calculated their  $E_{CD}$  and  $E_{VD}$  values. This expansion enables the model to capture features from a wider chemical space. However, the direct application of these properties as training targets exposed a fundamental challenge arising from severe distributional imbalances. As illustrated in **Fig. 4**, the raw distributions of  $E_{CD}$  and  $E_{VD}$  reveal two distinct patterns that present significant challenges for model training. The  $E_{CD}$  distribution is heavily skewed toward zero. Since most metallic materials lack an energy gap above the Fermi level, over 21,000 samples exhibit an  $E_{CD}$  of 0. In contrast, samples with non-zero  $E_{CD}$  values are sparsely distributed across the range greater than 0 eV, resulting in limited data density for learning meaningful features in these regions. Conversely, the  $E_{VD}$  distribution shows an opposing imbalance. While most metals have electronic states below the Fermi level, their  $E_{VD}$  values are predominantly concentrated in the high-energy region ( $>3$  eV), which accounts for over 22,000 samples. This distribution is

problematic because the region relevant for cold metal applications and the intermediate range (0–3 eV) are severely underrepresented, containing only a small fraction of the dataset.

To address these distributional imbalances, we introduce a unified descriptor termed the minimum band-edge distance,  $E_{\Delta,min}$ , defined as:

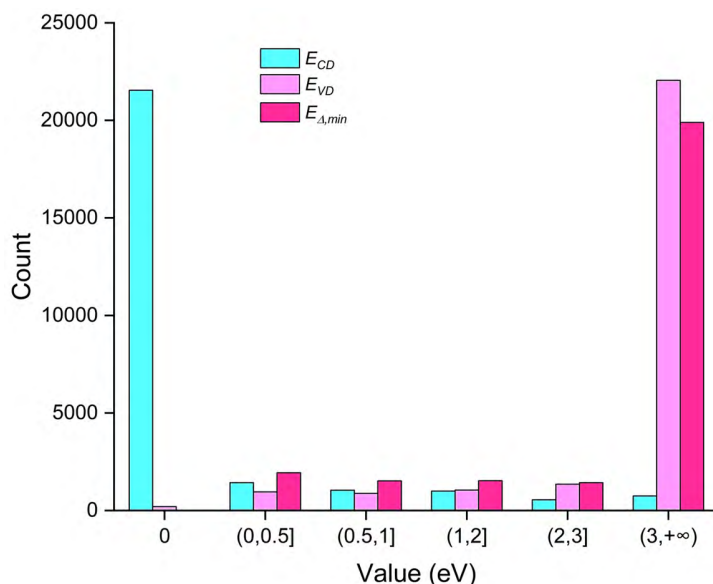
$$E_{\Delta,min} = \begin{cases} \min(|E_{CD}|, |E_{VD}|), & E_{CD} \neq 0 \text{ and } E_{VD} \neq 0 \\ |E_{CD}|, & E_{VD} = 0 \\ |E_{VD}|, & E_{CD} = 0 \end{cases} \quad (3)$$

where  $E_{CD}$  and  $E_{VD}$  denote the energy distances from  $E_F$  to the nearest edge of the cold-metal gap on the conduction side ( $E > E_F$ ) and valence side ( $E < E_F$ ), respectively. In this formulation, the minimization is conditional: if a gap is absent on one side (i.e., the value is 0), that component is excluded to isolate the active energy-filtering window. Consequently, for single-sided cold metals,  $E_{\Delta,min}$  reduces to the non-zero gap value. This construction naturally focuses training on materials with band-edge features near the Fermi level. As shown by the magenta bars in **Fig. 4**,  $E_{\Delta,min}$  exhibits a more balanced distribution. Compared to individual  $E_{CD}$  and  $E_{VD}$  distributions,  $E_{\Delta,min}$  provides substantially improved coverage in the low-energy regime (0–3 eV), with especially enhanced representation in the 0–0.5 eV range that contains the cold-metal screening window (50–500 meV).

We evaluated generative performance by training MatterGPT models on three property combinations: energy above hull (EAH) -  $E_{CD}$ , EAH -  $E_{VD}$ , and the unified EAH- $E_{\Delta,min}$ , generating equal numbers of structures from each. As shown in Table 1,  $E_{\Delta,min}$  exhibits the highest uniqueness (84.40%) and novelty (41.04%) among the three descriptors. Although it displays marginally lower symmetry (35.04%) than  $E_{VD}$  (36.19%), its superior performance in uniqueness and novelty justifies this minor trade-off. Based on these results, we constructed the final training dataset of 26,309 metallic materials labeled with EAH and  $E_{\Delta,min}$ . Training MatterGPT on this dataset enables systematic generation of cold metals with targeted electronic properties biased toward thermodynamic stability.

**Table 1.** Comparison of properties under different descriptors

Descriptor	Performance (%)		
	Uniqueness	Symmetry	Novelty
$E_{CD}$	79.30	16.36	32.87
$E_{VD}$	77.84	36.19	32.16
$E_{\Delta,min}$	<b>84.40</b>	35.04	<b>41.04</b>

**Fig. 4** |  $E_{CD}$ ,  $E_{VD}$  and  $E_{\Delta,min}$  distribution in the dataset. The null count for  $E_{\Delta,min}$  at 0 eV reflects the absence of materials in the dataset where both  $E_{CD}$  and  $E_{VD}$  vanish simultaneously.

## Discovery of new cold metal materials

Utilizing the trained MatterGPT model, we performed inverse design to generate cold metal candidates, targeting thermodynamic stability and  $E_{\Delta,min}$  within the 50-500 meV range. As illustrated in **Fig. 5**, the workflow begins by embedding these target properties, which condition the model to autoregressively generate SLICES sequences token by token. This process yielded 148,506 unique SLICES strings, each encoding the compositional and topological features of a potential cold metal. Subsequently, we converted these linear sequences into three-dimensional crystal structures using the SLI2Cry reconstruction algorithm. This conversion achieved a high

success rate of 92.1%, resulting in 136,766 valid structures. The few reconstruction failures were primarily attributed to invalid edge labels or topological inconsistencies in the generated sequences.

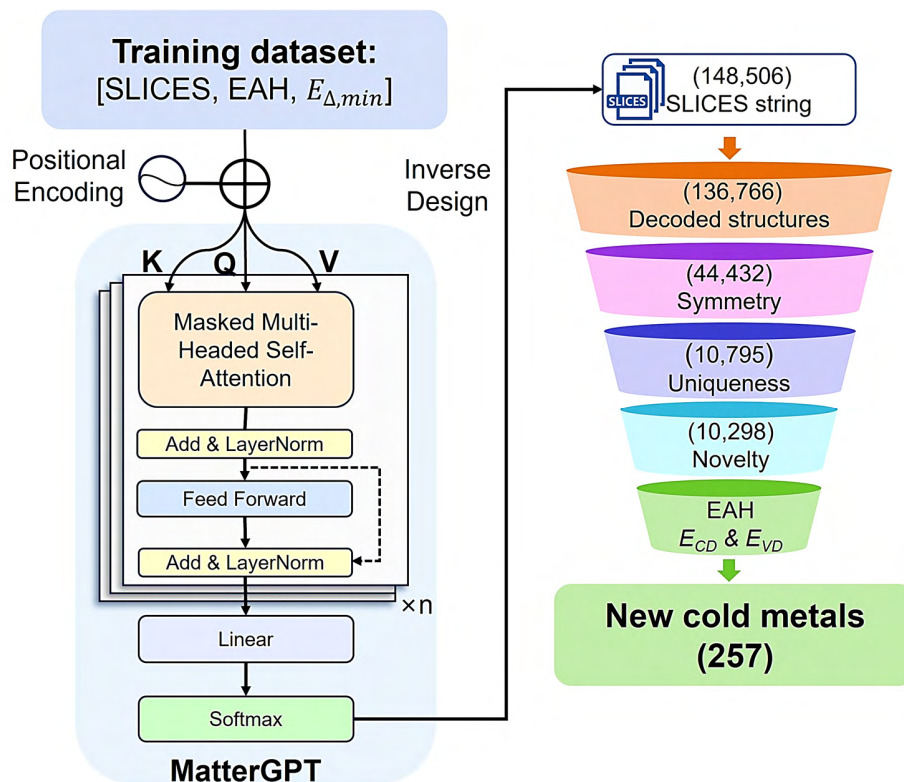


**Fig. 5** | Schematic overview of the MatterGPT-based inverse design workflow for generating novel cold metal candidates. Target properties, including EAH and  $E_{\Delta, min}$ , are embedded as conditioning inputs to guide the autoregressive generation of SLICES sequences. These sequences are subsequently converted into three-dimensional crystal structures via the reconstruction algorithm. The resulting candidates are then subjected to a three-stage screening protocol encompassing symmetry filtering, uniqueness verification, and novelty assessment against the Materials Project database, ultimately affording a pool of structurally valid and chemically novel cold metal candidates for further evaluation.

The reconstructed candidates were subjected to a rigorous three-stage screening protocol to ensure structural validity and novelty. First, we excluded structures assigned to the P1 space group to prioritize candidates with relatively high crystallographic symmetry for downstream analysis. Second, we evaluated uniqueness to eliminate redundant candidates produced within the same generative run. Following the methodology of Zeni et al. [45], we compared structures based on space groups and composition-normalized atomic coordinates—a robust approach dealing with

both ordered and disordered configurations. Finally, we assessed novelty by screening against the Materials Project [30] database. This verification ensures that the generated candidates represent previously unreported materials rather than reproductions of entries already catalogued in this comprehensive repository. This multi-stage pipeline refined the initial pool to 10,298 entirely novel candidates. All computational tasks, from training to generation, were performed on a workstation equipped with an Intel i9-10900KF processor and an NVIDIA RTX 3090 GPU (24 GB VRAM).

To evaluate the energy above hull and intrinsic cold metal characteristics of the 10,298 novel candidate structures, we performed high-throughput DFT calculations using VASP. This comprehensive assessment involved computing the energy above hull relative to known phases in the Materials Project database to quantify thermodynamic stability, while concurrently determining  $E_{CD}$  and  $E_{VD}$  values to confirm definitive cold metal features. Following Mal et al. [46], we retained only materials with  $E_{AH} < 0.25$  eV/atom, a threshold that identifies metastable yet experimentally accessible compounds. This final validation step reduced the candidate pool to 257 cold metals.

All validated candidates exhibit  $E_{CD}$  and/or  $E_{VD}$  values within the targeted 50-500 meV window, supporting their assignment as p-type, n-type, or np-type cold metals. Tables 2–4 present representative examples, whereas the complete validated data for these candidates are provided in Tables S1–S3 of the Supplementary Information. Notably, our generative approach differs fundamentally from previous high-throughput screening methods. While Zhang et al. [16] identified 252 cold metals by screening the Materials Project database, their strategy was inherently confined to previously documented materials. In contrast, our MatterGPT-based framework yielded 257 entirely novel compounds.

**Table 2.** p-type cold metals among candidate materials

<b>Formula</b>	<b>E<sub>AH</sub> (eV/atom)</b>	<b>E<sub>CD</sub> (eV)</b>	<b>E<sub>VD</sub> (eV)</b>	<b>Crystal system</b>
KTm <sub>2</sub> Sb <sub>2</sub> Se <sub>7</sub>	0.094	0.208	4.645	Orthorhombic
Na <sub>2</sub> CuRuF <sub>6</sub>	0.197	0.076	1.320	Cubic
CsBaF <sub>4</sub>	0.078	0.141	1.734	Tetragonal
CsNa <sub>2</sub> ZrI <sub>8</sub>	0.097	0.267	3.371	Trigonal
Sr <sub>2</sub> EuCoO <sub>6</sub>	0.142	0.358	2.400	Cubic

**Table 3.** n-type cold metals among candidate materials

Formula	EAH (eV/atom)	$E_{CD}$ (eV)	$E_{VD}$ (eV)	Crystal system
Nb <sub>2</sub> N <sub>3</sub> OF <sub>12</sub>	0.081	0.728	0.334	Monoclinic
Rb <sub>6</sub> SrCeCl <sub>12</sub>	0.104	2.258	0.116	Monoclinic
Na <sub>3</sub> MnCl <sub>5</sub>	0.107	2.614	0.278	Cubic
Cs <sub>2</sub> MnH <sub>7</sub>	0.052	1.201	0.300	Cubic
Rb <sub>3</sub> SeBr <sub>5</sub>	0.163	1.127	0.202	Tetragonal

**Table 4.** np-type cold metals among candidate materials

Formula	EAH (eV/atom)	$E_{CD}$ (eV)	$E_{VD}$ (eV)	Crystal system
Cs <sub>2</sub> TiCoF <sub>6</sub>	0.068	0.143	0.083	Cubic
Cs <sub>5</sub> CeF <sub>14</sub>	0.038	0.075	0.090	Monoclinic
YbCuF <sub>6</sub>	0.141	0.132	0.191	Trigonal
Na <sub>2</sub> TiNbCl <sub>8</sub>	0.091	0.240	0.349	Monoclinic
K <sub>2</sub> HgBiF <sub>6</sub>	0.226	0.441	0.123	Cubic

## Dynamic stability verification and electronic structure analysis

To validate the predicted properties and assess device application potential, we selected two representative p-type cold metal candidates from the 257 compounds discovered: CsBaF<sub>4</sub> ( $E_{CD} = 0.14$  eV, EAH = 0.08 eV/atom) and RbBaSe<sub>2</sub> ( $E_{CD} = 0.27$  eV, EAH = 0.22 eV/atom). We performed phonon dispersion calculations using the finite displacement method implemented in Phonopy [43] to confirm dynamical stability, following the computational protocols described in Section 2.3. Electronic band structure calculations were conducted to verify their intrinsic cold metal characteristics.

To further assess the suitability of the selected candidates for contact engineering, we evaluated their work functions using low-index surface slab models with symmetry-preserving terminations, since interfacial energy-level alignment is a key factor governing metal–semiconductor contact behavior [47]. In all calculations, vacuum regions thicker than 15 Å were introduced to suppress spurious interactions between periodic images. The work function was

determined from the difference between the vacuum level, extracted from the planar-averaged electrostatic potential in the vacuum region, and the Fermi level. As summarized in **Fig. 6**, both compounds exhibit contact-relevant work functions together with robust dynamical stability and the characteristic electronic signature of p-type cold metals. Specifically, the phonon dispersion curves in **Fig. 6c** and **Fig. 6g** show no imaginary modes throughout the Brillouin zone [48], confirming dynamical stability at 0 K, while the corresponding band structures in **Fig. 6b** and **Fig. 6f** reveal a distinct gap in the unoccupied states above the Fermi level, consistent with the defining feature of p-type cold metals.

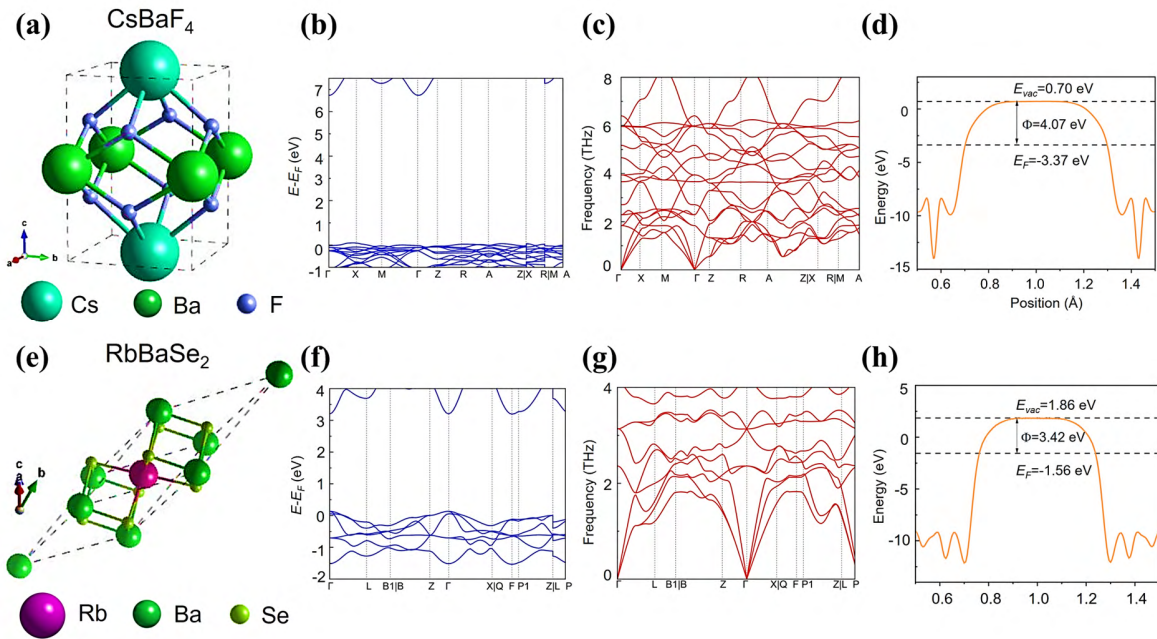


**Fig. 6** | Structural, dynamical, and electronic properties of two representative p-type cold metals. **(a)** Crystal structure of CsBaF<sub>4</sub>. **(b)** Electronic band structure of CsBaF<sub>4</sub>. **(c)** Phonon dispersion of CsBaF<sub>4</sub>. **(d)** Planar-averaged electrostatic potential of a representative surface slab of CsBaF<sub>4</sub>, yielding a work function of 4.07 eV. **(e)** Crystal structure of RbBaSe<sub>2</sub>. **(f)** Electronic band structure of RbBaSe<sub>2</sub>. **(g)** Phonon dispersion of RbBaSe<sub>2</sub>. **(h)** Planar-averaged electrostatic potential of a representative surface slab of RbBaSe<sub>2</sub>, yielding a work function of 3.41 eV. The dashed lines indicate the vacuum level and Fermi level.

Work function analysis yields  $\Phi = 4.07$  eV for CsBaF<sub>4</sub> (**Fig. 6d**) and  $\Phi = 3.41$  eV for RbBaSe<sub>2</sub> (**Fig. 6h**), respectively. These values fall comfortably within the work function window for cold-electron injection, aligning perfectly with the established energetic regimes of cold metals

reported in recent literature [16]. Notably, they closely match that of ZrRuSb (3.6 eV), which achieves subthreshold switching of 60 mV/decade in MoS<sub>2</sub> transistors [16]. This suggests similar potential for CsBaF<sub>4</sub> and RbBaSe<sub>2</sub> in cold electron injection applications. Their intrinsic band gaps of 50-500 meV above the Fermi level effectively filter high-energy carriers. This combination of favorable work functions and band-edge gap positioning makes CsBaF<sub>4</sub> and RbBaSe<sub>2</sub> strong candidates for steep-slope transistors and other low-power electronic devices. These findings validate that MatterGPT can generate novel cold metals with electronic properties matching those from high-throughput screening.

## Conclusion

We present an automated workflow for the inverse design of three-dimensional cold metals through generative artificial intelligence. In contrast to conventional high-throughput screening methods limited by finite material databases, our generative framework directly generates novel crystal structures with targeted electronic properties. We addressed the challenge of sparse training data by introducing a unified physical descriptor, the minimum band-edge distance  $E_{\Delta,min}$ . This descriptor consolidates the identification of p-type, n-type, and np-type cold metals into a single learning objective, enabling the MatterGPT model to generate target materials more efficiently.

By targeting thermodynamic stability and specific  $E_{\Delta,min}$  values, the model generated 148,506 candidate SLICES strings. We applied a multi-stage screening protocol involving structural reconstruction, novelty assessment, symmetry filtering, and high-throughput DFT calculations. This approach yielded 257 cold metal candidates with near-hull stability, none of which were matched to entries in the Materials Project database at the time of screening. First-principles validation of two representative p-type materials, CsBaF<sub>4</sub> and RbBaSe<sub>2</sub>, confirmed their dynamical stability via phonon dispersion analysis and verified their characteristic cold metal electronic structures. Both materials exhibit work functions of 4.07 eV and 3.41 eV, respectively, within the optimal range for semiconductor contact applications.

These results confirm that our approach can discover functional materials with targeted properties. The work makes two important contributions. It substantially expands the library of candidate cold metals for electronic applications, while their thermoelectric potential warrants future dedicated investigation. It also provides a viable computational framework for inverse design in sparsely populated target-property spaces. Future work should prioritize synthesis and

interface characterization of the most stable candidates, while improving generative diversity and accuracy through pre-training on larger crystal datasets and iterative DFT-in-the-loop refinement.

## **Declaration of Interest Statement**

The authors declare that they have no known competing financial interests or personal relationships that could have appeared to influence the work reported in this paper.

## **Acknowledgments**

This work was financially supported by the National Key Research and Development Program of China (Grant No.: 2024YFA1209801), the National Natural Science Foundation of China (Grant Nos.: 22203066, 12302140, and 12574265), the China Postdoctoral Science Foundation (Grant Nos.: 2023M732794 and 2025T180517), the Fundamental Research Funds for the Central Universities (Grant No.: sxzy012023213), and the Special Fund for AI-Empowered Scientific Research of the Shaanxi Provincial Department of Science and Technology (Grant No.: 2025YXYC012).

## **Data availability**

All data needed to evaluate the conclusions in the paper are present in the paper and/or the Supplementary Materials. The scripts that can generate the datasets, weights of the trained model, and related code can be found in the permanent Zenodo repository (<https://doi.org/10.5281/zenodo.18981860>).

## **Code availability**

The SLICES source code is available on GitHub (<https://github.com/xiaohang007/SLICES>). SLICES v2.0 was used in this work. Code and data for MatterGPT are available on GitHub (<https://github.com/xiaohang007/SLICES/tree/main/MatterGPT/>).

## References

- [1] E. Ko, J. Shin, C. Shin, Steep switching devices for low power applications: negative differential capacitance/resistance field effect transistors, *Nano Converg.* 5 (2018) 2.
- [2] X. Wang, Y. Chen, G. Wu, D. Li, L. Tu, S. Sun, H. Shen, T. Lin, Y. Xiao, M. Tang, others, Two-dimensional negative capacitance transistor with polyvinylidene fluoride-based ferroelectric polymer gating, *Npj 2D Mater. Appl.* 1 (2017) 38.
- [3] M. Si, C.-J. Su, C. Jiang, N.J. Conrad, H. Zhou, K.D. Maize, G. Qiu, C.-T. Wu, A. Shakouri, M.A. Alam, others, Steep-slope hysteresis-free negative capacitance MoS<sub>2</sub> transistors, *Nat. Nanotechnol.* 13 (2018) 24–28.
- [4] Y. Zhai, Z. Feng, Y. Zhou, S.-T. Han, Energy-efficient transistors: suppressing the subthreshold swing below the physical limit, *Mater. Horiz.* 8 (2021) 1601–1617.
- [5] T. Baba, Proposal for surface tunnel transistors, *Jpn. J. Appl. Phys.* 31 (1992) L455.
- [6] A.M. Ionescu, H. Riel, Tunnel field-effect transistors as energy-efficient electronic switches, *Nature* 479 (2011) 329–337.
- [7] S. Salahuddin, S. Datta, Use of negative capacitance to provide voltage amplification for low power nanoscale devices, *Nano Lett.* 8 (2008) 405–410.
- [8] J. Jo, C. Shin, Negative capacitance field effect transistor with hysteresis-free sub-60-mV/decade switching, *IEEE Electron Device Lett.* 37 (2016) 245–248.
- [9] K. Gopalakrishnan, P.B. Griffin, J.D. Plummer, Impact ionization MOS (I-MOS)-Part I: device and circuit simulations, *IEEE Trans. Electron Devices* 52 (2004) 69–76.
- [10] K. Gopalakrishnan, R. Woo, C. Jungemann, P.B. Griffin, J.D. Plummer, Impact ionization MOS (I-MOS)-part II: experimental results, *IEEE Trans. Electron Devices* 52 (2004) 77–84.
- [11] F. Liu, Switching at less than 60 mV/decade with a “cold” metal as the injection source, *Phys. Rev. Appl.* 13 (2020) 064037.
- [12] L. Zhang, G. Yao, X. Liu, F. Liu, Three-Dimensional Cold Metals in Realizing Steep-Slope Transistors Based on Monolayer MoS<sub>2</sub>, *IEEE Electron Device Lett.* 44 (2023) 1764–1767. <https://doi.org/10.1109/LED.2023.3305577>.
- [13] A. Kahn, Fermi level, work function and vacuum level, *Mater. Horiz.* 3 (2016) 7–10. <https://doi.org/10.1039/C5MH00160A>.
- [14] C.A. Mead, W.G. Spitzer, Fermi Level Position at Metal-Semiconductor Interfaces, *Phys. Rev.* 134 (1964) A713–A716. <https://doi.org/10.1103/PhysRev.134.A713>.
- [15] A. Zur, T.C. McGill, D.L. Smith, Fermi-level position at a semiconductor-metal interface, *Phys. Rev. B* 28 (1983) 2060. <https://doi.org/10.1103/PhysRevB.28.2060>.
- [16] L. Zhang, F. Liu, High-throughput approach to explore cold metals for electronic and thermoelectric devices, *Npj Comput. Mater.* 10 (2024) 78. <https://doi.org/10.1038/s41524-024-01267-w>.
- [17] X. Dong, H. Huang, L. Huang, Y. Zhou, B. Zhang, H. Zeng, Z. Lin, G. Zou, Unearthing Superior Inorganic UV Second-Order Nonlinear Optical Materials: A Mineral-Inspired

- Method Integrating First-Principles High-Throughput Screening and Crystal Engineering, *Angew. Chem. Int. Ed.* 63 (2024) e202318976.
- [18] M.Yu. Arsentev, E.I. Sysoev, A.I. Makogon, S.V. Balabanov, M.M. Sychev, M.H. Hammouri, V.A. Moshnikov, High-Throughput Screening of 3D-Printed Architected Materials Inspired by Crystal Lattices: Procedure, Challenges, and Mechanical Properties, *ACS Omega* 8 (2023) 24865–24874. <https://doi.org/10.1021/acsomega.3c00874>.
- [19] A. Benayad, D. Diddens, A. Heuer, A.N. Krishnamoorthy, M. Maiti, F.L. Cras, M. Legallais, F. Rahmanian, Y. Shin, H. Stein, M. Winter, C. Wölke, P. Yan, I. Cekic-Laskovic, High-Throughput Experimentation and Computational Freeway Lanes for Accelerated Battery Electrolyte and Interface Development Research, *Adv. Energy Mater.* 12 (2022) 2102678. <https://doi.org/10.1002/aenm.202102678>.
- [20] Y. Chung, Computation-Ready Experimental MOFs (CoRE MOFs), (2014) 80 Mb. <https://doi.org/10.11578/1118280>.
- [21] Z. Wang, F. You, Leveraging generative models with periodicity-aware, invertible and invariant representations for crystalline materials design, *Nat. Comput. Sci.* (2025) 1–12.
- [22] P.-P. De Breuck, H.-C. Wang, G.-M. Rignanese, S. Botti, M.A.L. Marques, Generative AI for crystal structures: a review, *Npj Comput. Mater.* 11 (2025) 370. <https://doi.org/10.1038/s41524-025-01881-2>.
- [23] S.R. Hall, F.H. Allen, I.D. Brown, The crystallographic information file (CIF): a new standard archive file for crystallography, *Acta Crystallogr. A* 47 (1991) 655–685. <https://doi.org/10.1107/S010876739101067X>.
- [24] L.M. Antunes, K.T. Butler, R. Grau-Crespo, Crystal structure generation with autoregressive large language modeling, *Nat. Commun.* 15 (2024) 10570. <https://doi.org/10.1038/s41467-024-54639-7>.
- [25] K. Choudhary, AtomGPT: Atomistic Generative Pretrained Transformer for Forward and Inverse Materials Design, *J. Phys. Chem. Lett.* 15 (2024) 6909–6917. <https://doi.org/10.1021/acs.jpcclett.4c01126>.
- [26] Z. Li, B. Cao, R. Jiao, L. Wang, D. Wang, Y. Liu, D. Chen, J. Li, Q. Liu, Y. Rong, L. Wang, T. Zhang, J.X. Yu, Materials Generation in the Era of Artificial Intelligence: A Comprehensive Survey, (2025). <https://doi.org/10.48550/arXiv.2505.16379>.
- [27] Z. Wang, H. Hua, W. Lin, M. Yang, K.C. Tan, Crystalline Material Discovery in the Era of Artificial Intelligence, (2026). <https://doi.org/10.48550/arXiv.2408.08044>.
- [28] Y. Chen, X. Wang, X. Deng, Y. Liu, X. Chen, Y. Zhang, L. Wang, H. Xiao, MatterGPT: A generative transformer for multi-property inverse design of solid-state materials, *ArXiv Prepr. ArXiv240807608* (2024).
- [29] H. Xiao, R. Li, X. Shi, Y. Chen, L. Zhu, X. Chen, L. Wang, An invertible, invariant crystal representation for inverse design of solid-state materials using generative deep learning, *Nat. Commun.* 14 (2023) 7027. <https://doi.org/10.1038/s41467-023-42870-7>.

- [30] A. Jain, S.P. Ong, G. Hautier, W. Chen, W.D. Richards, S. Dacek, S. Cholia, D. Gunter, D. Skinner, G. Ceder, K.A. Persson, Commentary: The Materials Project: A materials genome approach to accelerating materials innovation, *APL Mater.* 1 (2013). <https://doi.org/10.1063/1.4812323>.
- [31] D. Weininger, SMILES, a chemical language and information system. 1. Introduction to methodology and encoding rules, *J. Chem. Inf. Comput. Sci.* 28 (1988) 31–36. <https://doi.org/10.1021/ci00057a005>.
- [32] Z. Chen, Y. Yuan, S. Zheng, J. Guo, S. Liang, Y. Wang, Z. Wang, Transformer-Enhanced Variational Autoencoder for Crystal Structure Prediction, (2025). <https://doi.org/10.48550/arXiv.2502.09423>.
- [33] R. Wang, Y. Ji, Y. Li, S.-T. Lee, Applications of Transformers in Computational Chemistry: Recent Progress and Prospects, *J. Phys. Chem. Lett.* 16 (2024) 421–434.
- [34] S.P. Ong, W.D. Richards, A. Jain, G. Hautier, M. Kocher, S. Cholia, D. Gunter, V.L. Chevrier, K.A. Persson, G. Ceder, Python Materials Genomics (pymatgen): A robust, open-source python library for materials analysis, *Comput. Mater. Sci.* 68 (2013) 314–319. <https://doi.org/10.1016/j.commatsci.2012.10.028>.
- [35] N.E.R. Zimmermann, A. Jain, Local structure order parameters and site fingerprints for quantification of coordination environment and crystal structure similarity, *RSC Adv.* 10 (2020) 6063–6081. <https://doi.org/10.1039/C9RA07755C>.
- [36] S. Spicher, S. Grimme, Robust atomistic modeling of materials, organometallic, and biochemical systems, *Angew. Chem. Int. Ed.* 59 (2020) 15665–15673.
- [37] C. Chen, S.P. Ong, A universal graph deep learning interatomic potential for the periodic table, *Nat. Comput. Sci.* 2 (2022) 718–728.
- [38] W. Kohn, L.J. Sham, Self-Consistent Equations Including Exchange and Correlation Effects, *Phys. Rev.* 140 (1965) A1133–A1138. <https://doi.org/10.1103/PhysRev.140.A1133>.
- [39] P. Hohenberg, W. Kohn, Inhomogeneous Electron Gas, *Phys. Rev.* 136 (1964) B864–B871. <https://doi.org/10.1103/PhysRev.136.B864>.
- [40] G. Kresse, J. Furthmüller, Efficiency of ab-initio total energy calculations for metals and semiconductors using a plane-wave basis set, *Comput. Mater. Sci.* 6 (1996) 15–50. [https://doi.org/10.1016/0927-0256\(96\)00008-0](https://doi.org/10.1016/0927-0256(96)00008-0).
- [41] P.E. Blöchl, Projector augmented-wave method, *Phys. Rev. B* 50 (1994) 17953.
- [42] J.P. Perdew, K. Burke, M. Ernzerhof, Generalized Gradient Approximation Made Simple, *Phys. Rev. Lett.* 77 (1996) 3865–3868. <https://doi.org/10.1103/PhysRevLett.77.3865>.
- [43] A. Togo, I. Tanaka, First principles phonon calculations in materials science, *Scr. Mater.* 108 (2015) 1–5. <https://doi.org/10.1016/j.scriptamat.2015.07.021>.
- [44] L. Lin, R. Jacobs, T. Ma, D. Chen, J. Booske, D. Morgan, Work Function: Fundamentals, Measurement, Calculation, Engineering, and Applications, *Phys. Rev. Appl.* 19 (2023) 037001. <https://doi.org/10.1103/PhysRevApplied.19.037001>.

- [45] C. Zeni, R. Pinsler, D. Zügner, A. Fowler, M. Horton, X. Fu, Z. Wang, A. Shysheya, J. Crabbé, S. Ueda, R. Sordillo, L. Sun, J. Smith, B. Nguyen, H. Schulz, S. Lewis, C.-W. Huang, Z. Lu, Y. Zhou, H. Yang, H. Hao, J. Li, C. Yang, W. Li, R. Tomioka, T. Xie, A generative model for inorganic materials design, *Nature* 639 (2025) 624–632. <https://doi.org/10.1038/s41586-025-08628-5>.
- [46] S. Mal, G. Seal, P. Sen, MagGen: A Graph-Aided Deep Generative Model for Inverse Design of Permanent Magnets, *J. Phys. Chem. Lett.* 15 (2024) 3221–3228. <https://doi.org/10.1021/acs.jpcclett.4c00068>.
- [47] P. Schindler, E.R. Antoniuk, G. Cheon, Y. Zhu, E.J. Reed, Discovery of Stable Surfaces with Extreme Work Functions by High-Throughput Density Functional Theory and Machine Learning, *Adv. Funct. Mater.* 34 (2024) 2401764. <https://doi.org/10.1002/adfm.202401764>.
- [48] A. Togo, L. Chaput, I. Tanaka, Distributions of phonon lifetimes in Brillouin zones, *Phys. Rev. B* 91 (2015) 094306.

# Supplementary information

**Table S1. Complete list of validated p-type cold metal candidates**

Number	Formula	EAH (eV/atom)	$E_{CD}$ (eV)	$E_{VD}$ (eV)	$E_F$ (eV)	Crystal system
1	RbYbSe <sub>2</sub>	0.1912	0.3120	2.6389	0.4548	trigonal
2	Ba <sub>2</sub> YCoO <sub>6</sub>	0.1250	0.2764	2.1062	2.4463	cubic
3	NaYbSe <sub>2</sub>	0.1705	0.3971	3.1675	0.9318	tetragonal
4	Cs <sub>2</sub> RbYbCl <sub>6</sub>	0.1374	0.0815	0.6326	-1.8893	cubic
5	Ba <sub>2</sub> PrCoO <sub>6</sub>	0.1561	0.3387	2.0739	2.4639	cubic
6	Cs <sub>3</sub> YbCl <sub>6</sub>	0.1290	0.0863	1.4304	-1.8717	cubic
7	Ba <sub>2</sub> BiBr <sub>2</sub>	0.2209	0.3822	2.0353	2.4615	tetragonal
8	Ba <sub>2</sub> NaVO <sub>6</sub>	0.2034	0.3724	3.9167	1.5095	cubic
9	SrNdMnReO <sub>6</sub>	0.1806	0.3543	1.2130	5.5264	cubic
10	Na <sub>3</sub> CeSe <sub>6</sub>	0.1787	0.2420	2.2157	1.7431	cubic
11	K <sub>2</sub> RuBr <sub>7</sub>	0.1354	0.2016	2.4339	-0.1408	cubic
12	K <sub>2</sub> EuTiCl <sub>6</sub>	0.0522	0.4394	0.7296	-0.4977	cubic
13	Na <sub>3</sub> NbH <sub>6</sub>	0.1900	0.3104	0.5781	0.6140	cubic
14	Rb <sub>2</sub> NaCCl <sub>6</sub>	0.1118	0.1445	2.2667	-1.4935	cubic
15	Cs <sub>2</sub> KSrH <sub>6</sub>	0.2455	0.1567	2.3722	-1.1075	cubic
16	Ba <sub>2</sub> EuCoO <sub>6</sub>	0.0949	0.2662	2.2637	2.4348	cubic
17	Na <sub>2</sub> PdF <sub>7</sub>	0.2290	0.1026	0.5909	-2.2464	cubic
18	K <sub>2</sub> RbCaCl <sub>6</sub>	0.1518	0.0861	1.9245	-2.4118	cubic
19	KBa <sub>2</sub> BiN	0.2339	0.3716	2.0601	2.2023	cubic
20	K <sub>2</sub> TlFeCl <sub>6</sub>	0.1385	0.4281	1.0549	1.3695	cubic
21	Cs <sub>2</sub> NaSrCl <sub>6</sub>	0.1121	0.1192	1.9573	-1.4327	cubic
22	NbMo <sub>6</sub> Se <sub>8</sub>	0.1647	0.2351	6.3926	5.8664	trigonal
23	Rb <sub>2</sub> TlFeBr <sub>6</sub>	0.1243	0.4341	0.9389	0.9000	cubic
24	YbScF <sub>6</sub>	0.2371	0.1119	2.5083	-4.7933	trigonal
25	K <sub>2</sub> PdBr <sub>7</sub>	0.0753	0.2461	2.2820	-0.1768	cubic
26	Sr <sub>2</sub> CaVO <sub>6</sub>	0.1608	0.1477	1.7775	1.8997	cubic

Number	Formula	EAH (eV/atom)	$E_{CD}$ (eV)	$E_{VD}$ (eV)	$E_F$ (eV)	Crystal system
27	Cs <sub>2</sub> KYbCl <sub>6</sub>	0.1161	0.0972	0.7052	-1.7380	cubic
28	Sr <sub>2</sub> TbMnO <sub>6</sub>	0.0890	0.0923	2.1133	2.0609	cubic
29	TaInIr <sub>1</sub>	0.2332	0.3214	4.9135	6.6982	cubic
30	KSrSe <sub>2</sub>	0.2182	0.2662	2.0410	0.1556	trigonal
31	Cs <sub>2</sub> YbTlF <sub>6</sub>	0.0763	0.4503	0.6295	0.9554	cubic
32	BaZrV <sub>2</sub> O <sub>6</sub>	0.1384	0.3209	1.0076	5.0887	cubic
33	Ba <sub>2</sub> SmCoO <sub>6</sub>	0.1408	0.2941	2.0663	2.3440	cubic
34	K <sub>2</sub> SrTlF <sub>6</sub>	0.1705	0.4337	0.5368	0.4672	cubic
35	K <sub>2</sub> RuI <sub>7</sub>	0.1720	0.1507	2.3409	1.6080	cubic
36	NaYbSe <sub>2</sub>	0.1529	0.2600	3.0033	0.8659	trigonal
37	Sr <sub>2</sub> YbVO <sub>6</sub>	0.1761	0.1446	4.1439	1.6855	cubic
38	Sr <sub>3</sub> CoO <sub>6</sub>	0.2404	0.3819	2.0749	1.9390	cubic
39	Sr <sub>3</sub> NiO <sub>6</sub>	0.1664	0.4818	2.0290	1.8406	cubic
40	Rb <sub>2</sub> VCl <sub>7</sub>	0.1432	0.2086	0.5295	-0.0268	cubic
41	K <sub>2</sub> EuTiCl <sub>6</sub>	0.0316	0.0852	2.1590	-1.7862	cubic
42	Ba <sub>2</sub> SrCoO <sub>6</sub>	0.1745	0.2945	1.9314	2.0786	cubic
43	Cs <sub>2</sub> RbCaCl <sub>6</sub>	0.1374	0.0796	0.6400	-1.8207	cubic
44	Ba <sub>2</sub> NdCoO <sub>6</sub>	0.1476	0.2937	2.0494	2.3591	cubic
45	K <sub>2</sub> TiCuCl <sub>6</sub>	0.1379	0.3283	0.0437	2.8236	cubic
46	Ba <sub>2</sub> TbCoO <sub>6</sub>	0.1213	0.2957	2.0995	2.3517	cubic
47	Ba <sub>2</sub> DyCoO <sub>6</sub>	0.1195	0.2837	2.1404	2.4121	cubic
48	Ba <sub>2</sub> HoCoO <sub>6</sub>	0.1192	0.2907	2.1736	2.4061	cubic
49	K <sub>2</sub> YbTlF <sub>6</sub>	0.1326	0.4456	0.6244	0.5007	cubic
50	Cs <sub>2</sub> KRbF <sub>6</sub>	0.1304	0.2202	1.1867	-3.2444	cubic
51	Ba <sub>2</sub> GdCoO <sub>6</sub>	0.1123	0.2608	2.2125	2.4466	cubic
52	Ba <sub>3</sub> MnO <sub>6</sub>	0.1864	0.1119	1.6083	1.6057	cubic
53	Sr <sub>2</sub> EuCoO <sub>6</sub>	0.1417	0.3675	2.3958	2.5145	cubic
54	Cs <sub>2</sub> CoBr <sub>7</sub>	0.0988	0.1270	2.0530	0.0284	cubic
55	Cs <sub>2</sub> YbTiCl <sub>6</sub>	0.0568	0.2595	0.7378	0.5575	cubic

Number	Formula	EAH (eV/atom)	$E_{CD}$ (eV)	$E_{VD}$ (eV)	$E_F$ (eV)	Crystal system
56	Ba <sub>2</sub> CaVO <sub>6</sub>	0.1306	0.2642	1.6709	1.9929	cubic
57	Ba <sub>2</sub> YCoO <sub>6</sub>	0.1977	0.2744	4.7175	1.3843	cubic
58	K <sub>2</sub> GaPdF <sub>6</sub>	0.1432	0.1795	0.5051	1.3993	cubic
59	KCaSe <sub>2</sub>	0.2116	0.2305	2.3866	0.6279	trigonal
60	K <sub>2</sub> RbSnF <sub>6</sub>	0.1533	0.3709	0.6343	1.6069	cubic
61	K <sub>2</sub> MoBr <sub>7</sub>	0.1735	0.1344	0.6143	-0.3767	cubic
62	EuBi <sub>2</sub> Br <sub>3</sub>	0.2421	0.3915	3.2201	-0.6868	tetragonal
63	Ca <sub>2</sub> FeClO <sub>4</sub>	0.1713	0.3334	7.8364	3.7910	tetragonal
64	Ba <sub>2</sub> SrVO <sub>6</sub>	0.1804	0.2257	1.6208	1.8001	cubic
65	NaCaSe <sub>2</sub>	0.1964	0.2119	2.7939	1.1561	trigonal
66	Cs <sub>3</sub> YbF <sub>6</sub>	0.1379	0.0544	2.0857	-2.1527	cubic
67	Cs <sub>2</sub> KCaCl <sub>6</sub>	0.1206	0.0963	0.7126	-1.6744	cubic
68	Ba <sub>2</sub> YbCoO <sub>6</sub>	0.1637	0.3210	2.0420	2.0049	cubic
69	Cs <sub>2</sub> FeCuCl <sub>6</sub>	0.0794	0.1294	1.2005	1.8650	cubic
70	Ba <sub>2</sub> CaCoO <sub>6</sub>	0.1402	0.2674	2.0038	2.2325	cubic
71	Ba <sub>2</sub> ErCoO <sub>6</sub>	0.1194	0.2867	2.1893	2.3695	cubic
72	Ba <sub>2</sub> CaFeO <sub>6</sub>	0.1094	0.2687	1.8741	2.0555	cubic
73	K <sub>2</sub> YbTiCl <sub>6</sub>	0.1177	0.2783	0.7429	0.3415	cubic
74	Rb <sub>2</sub> EuTiCl <sub>6</sub>	0.0091	0.4079	0.7797	-0.6957	cubic
75	K <sub>2</sub> NaYbCl <sub>6</sub>	0.1334	0.2104	3.6718	-0.5566	cubic
76	Ba <sub>2</sub> ScCoO <sub>6</sub>	0.1329	0.2477	4.9532	1.7751	cubic
77	HfSbOs <sub>1</sub>	0.1045	0.1955	6.0432	6.8267	cubic
78	Rb <sub>3</sub> YbCl <sub>6</sub>	0.1409	0.0809	1.5039	-2.2511	cubic
79	Sr <sub>3</sub> MnO <sub>6</sub>	0.2457	0.1863	1.6583	1.5877	cubic
80	Cs <sub>2</sub> CuBr <sub>6</sub>	0.1054	0.4110	1.8586	0.1903	cubic
81	Sr <sub>3</sub> FeO <sub>6</sub>	0.2208	0.2847	2.0682	1.6632	cubic
82	K <sub>2</sub> NaYbF <sub>6</sub>	0.2102	0.0659	1.9239	-3.3228	cubic
83	Ca <sub>2</sub> W <sub>2</sub> O <sub>8</sub> F	0.1346	0.4674	6.1011	0.2129	monoclinic
84	BaVO <sub>4</sub>	0.1906	0.3862	3.6871	-0.0168	triclinic

Number	Formula	EAH (eV/atom)	$E_{CD}$ (eV)	$E_{VD}$ (eV)	$E_F$ (eV)	Crystal system
85	Cs <sub>3</sub> (CeSe <sub>3</sub> ) <sub>2</sub>	0.0676	0.0883	2.5624	1.0686	triclinic
86	TiCr <sub>2</sub> O <sub>6</sub>	0.1280	0.3981	0.6969	2.8777	triclinic
87	NaYbCl <sub>4</sub>	0.1511	0.3199	3.6308	-0.2724	triclinic
88	Cs <sub>7</sub> (PH) <sub>2</sub>	0.1106	0.1926	1.0177	1.7663	triclinic
89	K <sub>4</sub> Mn(CuBr <sub>4</sub> ) <sub>3</sub>	0.0400	0.2902	4.1913	0.6806	triclinic
90	CsLaF <sub>6</sub>	0.1340	0.3044	2.6875	-0.3419	monoclinic
91	Ce <sub>2</sub> Mo <sub>2</sub> O <sub>11</sub>	0.2226	0.4015	5.0650	1.2637	triclinic
92	Hg <sub>5</sub> F <sub>13</sub>	0.0256	0.4220	6.0966	-2.2052	triclinic
93	V <sub>3</sub> SiClO <sub>7</sub>	0.0871	0.3219	7.8255	3.9843	triclinic
94	KGeCl <sub>4</sub>	0.1802	0.3861	0.7721	0.3748	triclinic
95	CsRe <sub>2</sub> ICl <sub>8</sub>	0.1830	0.0708	1.2996	0.2212	triclinic
96	CsBaCu <sub>2</sub> F <sub>6</sub>	0.0978	0.1380	1.4455	1.1712	orthorhombic
97	BaVCrO <sub>6</sub>	0.1173	0.4861	0.5228	0.8880	triclinic
98	Dy <sub>3</sub> WO <sub>8</sub>	0.1441	0.2769	4.7536	0.9390	orthorhombic
99	K <sub>2</sub> Eu(OF <sub>3</sub> ) <sub>2</sub>	0.2036	0.0932	0.0024	-2.6264	triclinic
100	Na <sub>3</sub> LiF <sub>6</sub>	0.0446	0.4276	0.7597	-2.2045	monoclinic
101	Rb <sub>2</sub> AgCl <sub>6</sub>	0.0807	0.4366	1.9581	-0.3604	monoclinic
102	HgSeF <sub>5</sub>	0.1322	0.3246	0.7780	-0.8981	triclinic
103	CsNa <sub>2</sub> ZrI <sub>8</sub>	0.0973	0.2670	3.3709	0.8400	triclinic
104	CsTiF <sub>3</sub>	0.1999	0.3157	0.7482	5.0698	monoclinic
105	Y <sub>3</sub> Se <sub>3</sub> Br <sub>4</sub>	0.2074	0.2000	3.9765	0.0872	triclinic
106	Eu <sub>2</sub> OF <sub>4</sub>	0.0968	0.4032	0.6030	1.0172	triclinic
107	BaSrF <sub>6</sub>	0.0886	0.2696	3.3238	-1.5128	tetragonal
108	Cr <sub>2</sub> As <sub>3</sub> Se <sub>8</sub>	0.0201	0.4291	6.0308	3.3466	monoclinic
109	RbBaSe <sub>2</sub>	0.2195	0.2683	1.7284	-0.0349	trigonal
110	Cs <sub>3</sub> Te <sub>4</sub>	0.0973	0.2576	2.6671	1.7362	triclinic
111	K <sub>3</sub> YbF <sub>8</sub>	0.2240	0.2560	2.4540	-3.8948	monoclinic
112	KI <sub>2</sub>	0.0650	0.2589	5.3532	1.9796	triclinic
113	Na <sub>3</sub> EuF <sub>8</sub>	0.0005	0.1460	2.7200	-2.8007	monoclinic

Number	Formula	EAH (eV/atom)	$E_{CD}$ (eV)	$E_{VD}$ (eV)	$E_F$ (eV)	Crystal system
114	Cs <sub>2</sub> RuBr <sub>9</sub>	0.0798	0.1878	3.7825	-0.2755	triclinic
115	Cs <sub>4</sub> Se <sub>3</sub>	0.2197	0.2238	1.0124	0.2784	triclinic
116	Rb <sub>2</sub> CdAuF <sub>6</sub>	0.1181	0.3974	1.2345	-0.2490	cubic
117	Cs <sub>2</sub> SrF <sub>6</sub>	0.1624	0.2133	1.7071	-3.0575	triclinic
118	Tl(MoO <sub>4</sub> ) <sub>2</sub>	0.1894	0.2443	6.2122	0.8070	triclinic
119	CsBaF <sub>4</sub>	0.0783	0.1413	1.7337	-2.9746	tetragonal
120	Na <sub>2</sub> CuRuF <sub>6</sub>	0.1966	0.0760	1.3196	1.8970	monoclinic
121	CsRhBr <sub>6</sub>	0.1314	0.3619	1.8514	0.1149	triclinic
122	KTm <sub>2</sub> Sb <sub>2</sub> Se <sub>7</sub>	0.0940	0.2075	4.6448	2.5352	triclinic

**Table S2. Complete list of validated n-type cold metal candidates**

Number	Formula	EAH (eV/atom)	$E_{CD}$ (eV)	$E_{VD}$ (eV)	$E_F$ (eV)	Crystal system
1	K <sub>3</sub> ReF <sub>6</sub>	0.2200	0.0000	0.1434	2.8012	cubic
2	U <sub>2</sub> Cu <sub>2</sub> Se <sub>4</sub>	0.1763	0.0000	0.4399	2.8206	tetragonal
3	Cs <sub>2</sub> BaTbCl <sub>6</sub>	0.1334	0.0000	0.2473	3.9011	cubic
4	Cs <sub>2</sub> YbGdCl <sub>6</sub>	0.0475	0.0000	0.3058	4.5077	cubic
5	Rb <sub>3</sub> SeBr <sub>5</sub>	0.1630	1.1265	0.2024	-1.2836	tetragonal
6	Cs <sub>2</sub> YbTmCl <sub>6</sub>	0.1120	0.0000	0.2199	4.7484	cubic
7	Cs <sub>2</sub> YbNbF <sub>6</sub>	0.2067	0.0000	0.2804	3.8216	cubic
8	Cs <sub>2</sub> BaEuCl <sub>6</sub>	0.0159	0.0000	0.1156	2.7705	cubic
9	Rb <sub>2</sub> TiCl <sub>7</sub>	0.1084	0.7024	0.3280	-0.6678	cubic
10	Na <sub>2</sub> PrF <sub>7</sub>	0.0530	1.9340	0.1356	-3.2356	hexagonal
11	K <sub>2</sub> SrEuF <sub>6</sub>	0.0532	0.0000	0.3525	2.8619	cubic
12	KTbCl <sub>3</sub>	0.2139	0.0000	0.3698	3.8273	cubic
13	Cs <sub>2</sub> YbScF <sub>6</sub>	0.1369	0.0000	0.2573	5.4447	cubic
14	Cs <sub>2</sub> BaGdCl <sub>6</sub>	0.0872	0.0000	0.3278	3.6428	cubic
15	Cs <sub>2</sub> SrNbF <sub>6</sub>	0.2077	0.0000	0.2655	3.8547	cubic

Number	Formula	EAH (eV/atom)	$E_{CD}$ (eV)	$E_{VD}$ (eV)	$E_F$ (eV)	Crystal system
16	$K_2SrTiF_6$	0.1614	4.2154	0.4743	3.8836	cubic
17	$Na_3PrF_6$	0.1344	0.0000	0.2317	-3.6052	cubic
18	$EuFe_5O_8$	0.2384	0.0000	0.4011	3.6930	trigonal
19	$Cs_2YbPrCl_6$	0.0855	0.0000	0.3281	4.1677	cubic
20	$Rb_2NaTiCl_5$	0.1371	1.2278	0.3216	2.6226	cubic
21	$Cs_3NaTe_2Cl_4$	0.1765	1.3062	0.2471	0.6754	cubic
22	$Cs_2SrCeCl_6$	0.0864	0.0000	0.4568	4.5850	cubic
23	$Cs_2MnH_7$	0.0521	1.2009	0.3002	1.0540	cubic
24	$Cs_3NaCl_6$	0.0740	2.4334	0.2229	-2.2028	cubic
25	$Cs_2BaErCl_6$	0.1465	0.0000	0.2712	4.0040	cubic
26	$K_2TlSnF_6$	0.1441	0.9156	0.4534	2.1135	cubic
27	$Na_2TiCoF_6$	0.0999	0.0000	0.3708	3.6357	cubic
28	$RbTbCl_3$	0.1838	0.0000	0.4108	4.0237	cubic
29	$Rb_2YbErCl_6$	0.1253	0.0000	0.3066	4.3137	cubic
30	$BaEuCl_3$	0.2205	0.0000	0.4698	3.9453	hexagonal
31	$Cs_2BaEuCl_6$	0.0521	0.0000	0.0829	2.7726	cubic
32	$Rb_3TiCl_5$	0.1500	1.0307	0.2754	2.4234	cubic
33	$Cs_2BaLaCl_6$	0.1314	0.0000	0.4428	4.0717	cubic
34	$Cs_3FeCl_6$	0.1196	0.6175	0.4705	0.5869	cubic
35	$Cs_2KNaCoF_5$	0.1856	0.0000	0.1582	1.4014	cubic
36	$K_2TiF_7$	0.1278	1.2033	0.3146	-2.6696	cubic
37	$Rb_3NaF_6$	0.0492	0.5279	0.2062	-2.4913	cubic
38	$Na_3MnCl_5$	0.1071	2.6135	0.2777	-0.7632	cubic
39	$Cs_2TiTiF_6$	0.1660	1.4276	0.1980	1.1415	cubic
40	$Rb_2YbDyCl_6$	0.1190	0.0000	0.3359	4.2571	cubic
41	$Cs_2BaPrCl_6$	0.1307	0.0000	0.2868	3.6784	cubic

Number	Formula	EAH (eV/atom)	$E_{CD}$ (eV)	$E_{VD}$ (eV)	$E_F$ (eV)	Crystal system
42	Cs <sub>2</sub> TlF <sub>7</sub>	0.0546	1.3743	0.2393	-2.6280	cubic
43	Rb <sub>2</sub> RuAuCl <sub>6</sub>	0.1468	0.0000	0.3641	1.6882	cubic
44	Cs <sub>2</sub> Nb <sub>2</sub> Br <sub>6</sub>	0.1268	0.0000	0.4935	2.5848	hexagonal
45	K <sub>2</sub> TlWCl <sub>6</sub>	0.1281	0.0000	0.4223	1.9383	cubic
46	K <sub>2</sub> TiMnH <sub>6</sub>	0.2434	0.5231	0.3530	2.0811	cubic
47	Cs <sub>2</sub> YbNbCl <sub>6</sub>	0.1478	0.0000	0.4802	3.1325	cubic
48	Cs <sub>2</sub> SrGdCl <sub>6</sub>	0.0661	0.0000	0.4264	4.1789	cubic
49	Cs <sub>2</sub> SrPrCl <sub>6</sub>	0.1034	0.0000	0.2307	3.9208	cubic
50	Cs <sub>2</sub> YbHoCl <sub>6</sub>	0.1022	0.0000	0.2616	4.6766	cubic
51	Cs <sub>2</sub> TlCu <sub>2</sub> Cl <sub>5</sub>	0.0194	0.0000	0.2415	1.4093	cubic
52	SrNdFeCoO <sub>6</sub>	0.1729	0.8845	0.1535	3.2527	cubic
53	CeZr <sub>3</sub> TlSe <sub>8</sub>	0.1024	0.0000	0.0616	3.6985	triclinic
54	Ti <sub>2</sub> MnNbO <sub>7</sub>	0.0719	0.0000	0.4998	4.2190	triclinic
55	Sr <sub>4</sub> Br <sub>7</sub>	0.0676	0.0000	0.4476	4.0495	triclinic
56	Cs <sub>6</sub> IrAuCl <sub>10</sub>	0.0421	1.9832	0.2393	0.5206	triclinic
57	CsNa <sub>2</sub> InF <sub>6</sub>	0.0138	6.4548	0.3826	-2.8352	trigonal
58	CrP <sub>2</sub> Cl <sub>13</sub>	0.0548	0.7735	0.0901	0.7892	triclinic
59	Rb <sub>6</sub> SrCeCl <sub>12</sub>	0.1042	2.2581	0.1161	-0.9921	monoclinic
60	Rb <sub>2</sub> AlOF <sub>6</sub>	0.2461	0.6804	0.1185	-1.9396	triclinic
61	Cu <sub>2</sub> As <sub>2</sub> Cl <sub>7</sub>	0.1537	0.0000	0.1238	1.1664	triclinic
62	TiI <sub>2</sub> F <sub>9</sub>	0.1148	0.5458	0.1846	-0.6562	triclinic
63	CsCe <sub>3</sub> I <sub>8</sub>	0.0671	0.6716	0.1306	4.0857	triclinic
64	Na <sub>2</sub> ZrPbF <sub>10</sub>	0.0239	3.3729	0.2557	-3.1600	triclinic
65	Pr <sub>4</sub> SiBr <sub>7</sub>	0.1206	0.0000	0.1175	1.7535	triclinic
66	Cs <sub>2</sub> NbIF <sub>6</sub>	0.1360	0.8951	0.2108	0.2250	monoclinic
67	BaTi(ClF) <sub>2</sub>	0.1918	0.0000	0.1535	4.3505	monoclinic

Number	Formula	EAH (eV/atom)	$E_{CD}$ (eV)	$E_{VD}$ (eV)	$E_F$ (eV)	Crystal system
68	CaCePSe	0.1057	0.0000	0.3606	5.2432	trigonal
69	Rb <sub>4</sub> VCl <sub>7</sub>	0.0391	0.0385	0.4846	0.2064	monoclinic
70	Cs <sub>5</sub> Rb(MnCl <sub>5</sub> ) <sub>2</sub>	0.0108	2.7635	0.3603	0.1045	triclinic
71	Ce <sub>5</sub> CCl <sub>8</sub>	0.0899	0.0000	0.4187	3.8776	monoclinic
72	Cs <sub>5</sub> Nb <sub>2</sub> F <sub>12</sub>	0.0725	0.5633	0.1226	0.8441	triclinic
73	Ti <sub>2</sub> OF <sub>5</sub>	0.1842	3.3761	0.1640	1.3161	triclinic
74	ScTiCl <sub>3</sub>	0.2146	0.0000	0.4193	4.9824	monoclinic
75	Cs <sub>6</sub> RbCr <sub>2</sub> Br <sub>11</sub>	0.0818	1.3602	0.3195	0.4614	triclinic
76	Na <sub>3</sub> GdF <sub>6</sub>	0.1868	0.0000	0.2688	-1.8745	monoclinic
77	TiMn <sub>2</sub> CdI <sub>8</sub>	0.0737	0.0000	0.4933	2.4928	triclinic
78	Cs <sub>3</sub> C <sub>2</sub> N <sub>3</sub>	0.0699	0.0000	0.4466	1.0025	triclinic
79	Na <sub>2</sub> Mn <sub>3</sub> VO <sub>6</sub>	0.0775	0.0000	0.1682	4.7790	monoclinic
80	Rb <sub>2</sub> ZrHgF <sub>6</sub>	0.1287	0.0000	0.4126	-0.9915	cubic
81	Ba <sub>3</sub> CeBr <sub>8</sub>	0.0713	0.0000	0.4629	4.9212	triclinic
82	NbICl <sub>8</sub>	0.0593	2.0986	0.1926	-0.8564	triclinic
83	Mo <sub>3</sub> (AsCl <sub>4</sub> ) <sub>2</sub>	0.1938	0.0334	0.0685	-0.1655	triclinic
84	Sc <sub>2</sub> SBr <sub>3</sub>	0.2134	0.0000	0.3689	3.1644	monoclinic
85	Rb <sub>2</sub> PtF <sub>7</sub>	0.1090	0.0445	0.3369	-2.0210	cubic
86	Cs <sub>3</sub> Er <sub>2</sub> Cl <sub>7</sub>	0.1584	0.0000	0.4770	4.3760	triclinic
87	Sr <sub>7</sub> Mn(SO) <sub>4</sub>	0.1793	0.0000	0.2225	2.0997	triclinic
88	Nb <sub>2</sub> N <sub>3</sub> OF <sub>12</sub>	0.0808	0.7279	0.3341	-4.2838	triclinic

**Table S3. Complete list of validated np-type cold metal candidates**

Number	Formula	EAH (eV/atom)	$E_{CD}$ (eV)	$E_{VD}$ (eV)	$E_F$ (eV)	Crystal system
1	Cs <sub>2</sub> UCuCl <sub>6</sub>	0.1908	0.0502	0.1112	4.5024	cubic
2	Cs <sub>3</sub> KF <sub>6</sub>	0.1010	0.1875	0.1843	-2.4476	cubic

Number	Formula	EAH (eV/atom)	$E_{CD}$ (eV)	$E_{VD}$ (eV)	$E_F$ (eV)	Crystal system
3	Cs <sub>2</sub> TiCoF <sub>6</sub>	0.0678	0.1429	0.0830	3.2058	cubic
4	Tl <sub>2</sub> Ni <sub>2</sub> Cl <sub>4</sub>	0.1970	0.2084	0.3731	2.3081	hexagonal
5	K <sub>3</sub> ReCl <sub>6</sub>	0.1755	0.2881	0.1314	2.1202	cubic
6	Cs <sub>2</sub> TiCuCl <sub>6</sub>	0.1637	0.1322	0.0834	3.1331	cubic
7	K <sub>2</sub> TiFeF <sub>6</sub>	0.0065	0.0589	0.1405	3.6614	cubic
8	Na <sub>3</sub> EuF <sub>6</sub>	0.1051	0.1037	0.1015	-1.8764	cubic
9	Rb <sub>3</sub> TaCl <sub>6</sub>	0.1578	0.1244	0.2370	2.2875	cubic
10	Sr <sub>2</sub> Pd <sub>2</sub> F <sub>6</sub>	0.1551	0.2642	0.2286	2.0063	cubic
11	K <sub>2</sub> PdF <sub>7</sub>	0.1133	0.0690	0.4489	-2.5773	cubic
12	Cs <sub>2</sub> YbTiCl <sub>6</sub>	0.0532	0.1391	0.2965	3.5518	cubic
13	Cs <sub>2</sub> PdF <sub>7</sub>	0.0845	0.1391	0.2171	-2.3962	cubic
14	K <sub>2</sub> TiNiF <sub>6</sub>	0.0356	0.2166	0.3386	3.6806	cubic
15	Cs <sub>2</sub> NaFeCl <sub>6</sub>	0.1658	0.3128	0.4179	-1.0512	cubic
16	SrPr <sub>2</sub> VO <sub>6</sub>	0.1277	0.2428	0.2256	4.1520	cubic
17	Rb <sub>2</sub> PdF <sub>7</sub>	0.0968	0.2815	0.2783	-2.7444	cubic
18	Rb <sub>2</sub> TiCoF <sub>6</sub>	0.0154	0.1982	0.4443	3.8320	cubic
19	K <sub>2</sub> RbEuCl <sub>6</sub>	0.1456	0.1927	0.0557	-2.3383	cubic
20	K <sub>2</sub> SrRhF <sub>6</sub>	0.2301	0.1137	0.1675	1.7712	cubic
21	K <sub>2</sub> RbEuCl <sub>6</sub>	0.0353	0.0601	0.2239	-2.3738	cubic
22	Rb <sub>2</sub> TiCuCl <sub>6</sub>	0.1421	0.2216	0.1945	2.8617	cubic
23	Rb <sub>3</sub> NbH <sub>6</sub>	0.1398	0.0880	0.3540	0.3711	cubic
24	Na <sub>3</sub> OsF <sub>6</sub>	0.2283	0.1729	0.2589	1.6368	cubic
25	Cs <sub>2</sub> CuRuF <sub>6</sub>	0.1587	0.0641	0.0750	2.1688	cubic
26	Cs <sub>2</sub> TiTiF <sub>6</sub>	0.0985	0.2372	0.1678	3.9032	cubic
27	Cs <sub>2</sub> Se <sub>6</sub>	0.1899	0.4995	0.2809	-2.2358	tetragonal
28	BaIr <sub>2</sub> F <sub>11</sub>	0.0005	0.0978	0.0628	-0.2099	triclinic

Number	Formula	EAH (eV/atom)	$E_{CD}$ (eV)	$E_{VD}$ (eV)	$E_F$ (eV)	Crystal system
29	Ce <sub>3</sub> Br <sub>8</sub>	0.0092	0.2752	0.1593	2.5882	triclinic
30	Hg <sub>3</sub> PF <sub>6</sub>	0.1217	0.4351	0.4604	-1.7733	triclinic
31	Cs <sub>2</sub> OsIBr <sub>5</sub>	0.0208	0.2611	0.2058	0.9388	monoclinic
32	Na <sub>2</sub> TiNbF <sub>8</sub>	0.1593	0.0866	0.0795	3.3847	tetragonal
33	Ho <sub>7</sub> RuI <sub>12</sub>	0.0165	0.1061	0.4759	4.1065	triclinic
34	Rb <sub>2</sub> YbAgF <sub>6</sub>	0.0501	0.2926	0.1981	-1.0262	monoclinic
35	Eu <sub>2</sub> O <sub>2</sub> F <sub>3</sub>	0.1400	0.0833	0.4510	1.5764	monoclinic
36	K <sub>6</sub> EuMn <sub>3</sub> O <sub>8</sub>	0.0813	0.0536	0.0913	1.8412	triclinic
37	Ce <sub>2</sub> TiNiO <sub>6</sub>	0.2144	0.0545	0.1563	7.6760	trigonal
38	K <sub>5</sub> (CoCl <sub>4</sub> ) <sub>3</sub>	0.0539	0.1584	0.0726	0.5593	triclinic
39	KRb <sub>3</sub> Ag <sub>2</sub> F <sub>12</sub>	0.0112	0.0729	0.3107	-2.9547	triclinic
40	Na <sub>2</sub> TiNbCl <sub>8</sub>	0.0913	0.2401	0.3489	2.4505	triclinic
41	Cs <sub>2</sub> KF <sub>7</sub>	0.0835	0.0678	0.0800	-3.1409	monoclinic
42	Ce <sub>4</sub> NCl <sub>6</sub> O	0.0730	0.0886	0.0734	6.6431	triclinic
43	HgIrF <sub>8</sub>	0.0541	0.4476	0.3944	-2.5553	triclinic
44	Rb <sub>2</sub> IrPdF <sub>6</sub>	0.2123	0.2831	0.3740	1.2458	monoclinic
45	Rb <sub>2</sub> CaF <sub>7</sub>	0.2018	0.0874	0.2253	-3.2065	triclinic
46	YbCuF <sub>6</sub>	0.1408	0.1323	0.1913	-2.5946	trigonal
47	Cs <sub>5</sub> CeF <sub>14</sub>	0.0375	0.0751	0.0896	-2.6675	triclinic